







Nanostructured front electrodes for perovskite/c-Si tandem photovoltaics

IHTEAZ M. HOSSAIN,^{1,2,4,5}  YIDENEKACHEW J. DONIE,^{1,2,4}
RAPHAEL SCHMAGER,¹  MOHAMED S. ABDELKHALIK,¹ MICHAEL
RIENÄCKER,³ TOBIAS F. WIETLER,³ ROBBY PEIBST,³ ANDREI
KARABANOV,² JONAS A. SCHWENZER,² SOMAYEH
MOGHADAMZADEH,^{1,2} ULRICH LEMMER,^{1,2} BRYCE S.
RICHARDS,^{1,2}  GUILLAUME GOMARD,^{1,2} AND ULRICH W.
PAETZOLD^{1,2,6} 

¹*Institute of Microstructure Technology, Karlsruhe Institute of Technology, Hermann-von-Helmholtz-Platz 1, 76344, Germany*

²*Light Technology Institute, Karlsruhe Institute of Technology, Engesserstr. 13, 76131 Karlsruhe, Germany*

³*Institute for Solar Energy Research in Hamelin (ISFH), Am Ohrberg 1, D-31860 Emmerthal, Germany*

⁴*Co-first authors with equal contribution*

⁵*ihateaz.hossain@kit.edu*

⁶*ulrich.paetzold@kit.edu*

Abstract: The rise in the power conversion efficiency (PCE) of perovskite solar cells has triggered enormous interest in perovskite-based tandem photovoltaics. One key challenge is to achieve high transmission of low energy photons into the bottom cell. Here, nanostructured front electrodes for 4-terminal perovskite/crystalline-silicon (perovskite/c-Si) tandem solar cells are developed by conformal deposition of indium tin oxide (ITO) on self-assembled polystyrene nanopillars. The nanostructured ITO is optimized for reduced reflection and increased transmission with a tradeoff in increased sheet resistance. In the optimum case, the nanostructured ITO electrodes enhance the transmittance by ~7% (relative) compared to planar references. Perovskite/c-Si tandem devices with nanostructured ITO exhibit enhanced short-circuit current density (2.9 mA/cm² absolute) and PCE (1.7% absolute) in the bottom c-Si solar cell compared to the reference. The improved light in-coupling is more pronounced for elevated angle of incidence. Energy yield enhancement up to ~10% (relative) is achieved for perovskite/c-Si tandem architecture with the nanostructured ITO electrodes. It is also shown that these nanostructured ITO electrodes are also compatible with various other perovskite-based tandem architectures and bear the potential to improve the PCE up to 27.0%.

Published by The Optical Society under the terms of the [Creative Commons Attribution 4.0 License](https://creativecommons.org/licenses/by/4.0/). Further distribution of this work must maintain attribution to the author(s) and the published article's title, journal citation, and DOI.

1. Introduction

During the last decade, organo-metal halide perovskite solar cells (PSCs) have witnessed a remarkable enhancement in the power conversion efficiency (PCE), surpassing 25% to date [1]. Perovskite thin-films possess excellent opto-electronic properties for photovoltaics, namely high absorption coefficient and long carrier diffusion length [2,3]. Additionally, their bandgap can be tuned by compositional engineering of the perovskite crystal components [4]. This feature makes PSCs versatile candidates for tandem devices in conjunction with low-bandgap single-junction crystalline-silicon (c-Si) or copper indium gallium diselenide (CIGS) solar cells. Although the theoretical limit in the PCE of perovskite/c-Si tandem solar cells is 45.3%, real prototype devices fall far short of this limit and the PCE of these current state-of-the-art tandem solar cells is still

< 33% [5–13]. This is due to a variety of optical and electrical losses such as reflection losses at the interfaces, reduced transmission of the top cell due to the parasitic absorption within the layers, non-radiative recombination losses at the interface of the charge carriers and poor fill factors (FF) due to imperfect charge transport [14–18].

A number of light management concepts have been investigated in order to overcome the optical losses for both perovskite-based tandems and single-junction PSCs [14]. Micron-scale textures at the front side of two-terminal (2 T) and four-terminal (4 T) device architectures have demonstrated to reduce the reflection losses, improving the light in-coupling and light trapping as well as enhancing the transmission of the low energy photons through the top solar cell into the bottom solar cell [8,9,14,19–22]. Excellent light harvesting was demonstrated in textured 2 T perovskite/c-Si tandem solar cells with PCE exceeding 25% using a fabrication process of the perovskite absorber layer that involved both co-evaporation and spin coating deposition techniques [19]. An alternative strategy, mostly employed so far in 4 T architectures having front planar surfaces, but also compatible with 2 T, makes use of retroreflector-inspired micron-scale pyramidal structures or micro-textured foils at the front side of the transparent cover of the device [8,9,20,22]. These micro-textures reduce the reflection losses of the incident light by multiple interactions with the textured surface, which increases the probability for light in-coupling [23,24]. Further improvements are also possible through retroreflections of well-designed micro-textures [25]. Exceptional device performance with PCE exceeding 26% was demonstrated by these textures [8]. Next to micron-scale textures, nano-scale textures have also been demonstrated to improve light in-coupling and light trapping in PSCs [26–37]. To date they have been mostly implemented in opaque PSCs, however, the concepts are widely transferable to semi-transparent PSCs and tandem architectures. The prototyped nano-scale textures encompass nanophotonic front and rear electrodes, patterned charge transport and active perovskite layers, as well as corrugated substrates [28–37]. The patterned active layers enhance the coupling of light into quasi-guided modes in the active medium, thus improving the absorption. The rear electrode improves absorption of light through scattering and surface plasmonic resonance excited by the corrugation [32]. In regard to nanophotonic front electrodes, proposed textured surface reduces the reflection losses by introducing an effective refractive index medium, thus suppressing the Fresnel reflection losses [30,33]. The nanophotonic front electrode is of particular interest as it not only textures the transparent conductive oxide (TCO) but also the electron transport layer (ETL) and the perovskite absorber layer. Thus, texturing the TCO promises to reduce the reflection losses of 5–20% at the glass/ITO/ETL/perovskite interfaces, which is mostly due to the change in the optical indices at the various interfaces. Previously, patterned ITO with periodic structures demonstrated enhanced short-circuit current density (J_{SC}) of 5% (relative), leading to an enhancement in PCE of ~3% (relative) compared to planar reference devices [30]. In another study, Khan *et al.* developed ITO films atop periodically corrugated substrate and demonstrated excellent optical transmittance over both the visible and near-infrared ranges [38]. This work was carried out with stand-alone configurations; therefore, the beneficial impact of nanostructured front electrodes with improved optical properties is still to be tested in functional semi-transparent PSCs and perovskite-based tandem photovoltaics.

In this study, nanostructured ITO (NS ITO) electrodes are developed aiming to reduce the reflection losses at the glass/ITO/ETL/perovskite interfaces. Nanostructured front electrodes are optimized that demonstrate enhanced light in-coupling and transmission over a wide spectral range. Semi-transparent PSCs fabricated on these nanostructured electrodes are combined with c-Si bottom solar cells to form 4 T tandem architectures, which exhibit enhanced current generation and PCE compared to planar references. In addition, the 4 T PSC/c-Si tandem solar cells using nanostructured front electrodes show improved angular stability of light in-coupling, leading to an enhanced annual energy yield.

2. Experimental

2.1. Device fabrication

For the fabrication of semi-transparent PSCs, 16 mm x 16 mm glass substrates were cleaned using ultrasonic baths of acetone and isopropanol for 10 min each. Afterwards, the samples were cleaned with deionized water for 20 s and dried with N₂. The polystyrene nanopillars were fabricated with polymer blend lithography. A schematic (see Fig. 4) of the various steps in the fabrication process is illustrated in the appendix. A blend of polystyrene (PS, molecular weight: 3.25k, Sigma Aldrich) and poly(methyl methacrylate) (PMMA, molecular weight: 5.50k, Sigma Aldrich) dissolved in methyl ethyl ketone (MEK, Sigma Aldrich) solvent in a mass ratio of 4/6, 15 mg/ml concentration was used. In order to dissolve the mixture quickly, the solution was placed on a hot plate at 100 °C for an hour. Then, a 40 µl aliquot was spin-coated onto the glass substrate at a speed of 3000 rpm for 30 s (humidity ~45%). After the spin coating, the samples were exposed to O₂ plasma for 30 s at a power of 50 W. The sample was then developed using acetic acid (concentration of 99%, Alfa Aesar) that removed the PMMA. The ITO layers were sputtered using a Kurt J. Lesker PVD-75 thin film deposition system. For the deposition of ~135 nm ITO, the following parameters were used: power = 50 W, temperature = 25 °C, deposition time = 2000 s, pressure = 0.8 mTorr, and O₂ partial pressure = 2.5%. The samples were annealed for 30 min at 200 °C on a hot plate that improved both the transmission and the conductivity. SnO₂-np (Alfa Aesar) was spin-coated at a speed of 4000 rpm for 30 s, followed by an annealing step at 200 °C for 30 min in air. The SnO₂-np solution was obtained after diluting it to a concentration of ~2.5% from an original concentration of 15%. For the batch 1, a ~400 nm perovskite absorber layer was deposited by an anti-solvent approach. The perovskite absorber solution was prepared from the precursors of methylammonium bromide (MABr, Great Cell Solar), formamidinium iodide (FAI, Great Cell Solar), lead iodide (PbI₂, TCI) and lead bromide (PbBr₂, TCI) in 0.2 M, 1 M, 1.1 M, and 0.2 M, respectively, dissolved in the solvent ratio 4:1 of N,N-Dimethylformamide (DMF, Sigma Aldrich) and dimethyl sulfoxide (DMSO, Sigma Aldrich). 88.9 µL of CsI (Alfa Aesar) solution (1.5 M in DMSO) was added to form Cs_{0.1}(MA_{0.17}FA_{0.83})_{0.9}Pb(I_{0.83}Br_{0.17})₃. The absorber layer was obtained by spin coating in a two-step process: (1000 rpm for 10 s and 6000 rpm for 20 s). During the second spin coating step, chlorobenzene (Sigma Aldrich) was released as the anti-solvent, 5–7 s prior to the end of the step. The samples were annealed at 100 °C for 1 h inside the glovebox. For the batch 2, FA_{0.71}MA_{0.29}PbI_{2.87}Br_{0.13} perovskite was deposited. Lead iodide (Alfa Aesar) was spin-coated from a 1.2 M solution in DMF:DMSO (19:1) at 1500 rpm for 30 s in a nitrogen filled glovebox. Subsequently, the substrate was heated to 70 °C for one minute. Then, a solution containing FAI, MABr, and methylammonium chloride (Dyesol) in a concentration of 60 mg/ml, 6 mg/ml, and 6 mg/ml respectively, was spin-coated at 1300 rpm for 30 s in nitrogen atmosphere followed by 15 minutes of annealing at 150 °C under ambient conditions. For the ~200 nm thick hole transport layer, 2,2',7,7'-tetrakis[N,N-di(4-methoxyphenyl)amino]-9,9'-spirobifluorene (spiro-MeOTAD, Lumtec) solution (80 gm in 1 ml of chlorobenzene, doped with 17.5 µl of lithium salt solution and 28.5 µl 4-tetra-butylpyridine (Sigma Aldrich) was spin-coated at 4000 rpm for 30 s inside the glovebox. The lithium salt solution was prepared from 520 mg of lithium bis(trifluoromethanesulfonyl) imide (Sigma Aldrich) in 1 ml acetonitrile (Sigma Aldrich). The substrates were exposed for the oxygen doping for at least 12 h in a dry box (25-30% humidity). 10 nm of MoO_x (Sigma Aldrich) was evaporated using Lesker Spectros PVD system at a rate of 0.8 Å/s at 6 × 10⁻⁶ mbar pressure. The ~150 nm thick ITO electrodes were sputtered with the following parameters: power= 50 W, temperature = 25 °C, deposition time = 2300 s, pressure = 0.8 mTorr, and O₂ partial pressure = 2.5%. The active area of the fabricated cells is 10.5 mm².

For the fabrication of c-Si solar cell, a shiny-etched 6-inch p-type Floatzone (FZ) silicon wafers was used with a base resistivity of $1.5 \Omega\text{cm}$ and a thickness of $300 \mu\text{m}$ as substrate material and 27 small cells with an active cell area of $7.6 \times 15.5 \text{ mm}^2$ on each wafer was fabricated mostly following the cell process in Ref. [39,40]. After growing a $\sim 2.1 \text{ nm}$ thin thermal silicon dioxide layer in a tube furnace, undoped amorphous silicon (a-Si) was deposited on both sides by using low pressure chemical vapor deposition (LPCVD). Hereafter the front (rear) side of the wafer received a blanket phosphorus (boron) implantation, followed by a masked phosphorus implantation on the rear. The latter locally overcompensated the boron in an interdigitated pattern with a pitch of $950 \mu\text{m}$. For the masking of the phosphorus implantation, a sputtered dielectric layer was patterned by inkjet-printed hotmelt wax and a subsequent wet-chemical etching. After removal of the dielectric implant mask, high temperature treatment for the formation of the POLO junctions was performed at $1035 \text{ }^\circ\text{C}$ for 60 min. During this step, a thick SiO_2 layer was grown on top of the poly-Si by wet thermal oxidation. Subsequently, this SiO_2 layer was again patterned via inkjet printing on the rear, and removed from the front side of the wafer. The remaining SiO_2 on the rear acts as etching barrier for a subsequent texturization process, which yields a textured front side and a separation of n^+ and p^+ poly-Si regions by a textured trench. After removing the SiO_2 mask, the cell precursors were passivated with an $\text{AlO}_x/\text{SiN}_y$ double layer on both sides. The SiN_x layers have a refractive index of 2.4 and a thickness of about 60 - 70 nm on the front and 30 nm on the rear side. On the front side, the $\text{AlO}_x/\text{SiN}_y$ anti-reflection coating was optimized for the integration in a 4 T tandem cell by stacking top and bottom cell with epoxy [41,42]. A significant loss in short-circuit current density (J_{SC}) due to reflection and parasitic absorption in the SiN_x layer is expected, if the bottom cell is measured as a single-junction cell under AM 1.5G conditions. In order to optimize the infrared response of the bottom cell, a 200 nm-thick silicon dioxide layer was deposited on the rear side using plasma-enhanced chemical vapour deposition (PECVD). Dielectric layers were created via contact openings in the rear side by selectively laser ablating the $\text{SiO}_2/\text{SiN}_y$ layer stack from the poly-Si. Subsequently, the AlO_x was removed using a short HF treatment prior to aluminum metallization of the rear side by vacuum evaporation in an industrial high-throughput tool from Applied Materials. A self-aligned RISE contact separation and cleaving the cells from the substrate completed the cell process.

2.2. Characterization

The solar cells were characterized using a class AAA Newport solar simulator (xenon lamp). The measurements for the PSCs were carried out under AM 1.5G conditions for open-circuit voltage (V_{OC}) to short-circuit current density (J_{SC}) and J_{SC} to V_{OC} at a fixed rate of 600 mV/s using a Keithley 2400 source meter. The temperature ($25 \text{ }^\circ\text{C}$) of the PSC was controlled actively using a Peltier element control circuit. The top PSCs were measured with an aperture area of 5.6 mm^2 . The c-Si solar cell was measured either stand-alone or under the filters of planar ITO-PSC and NS ITO-PSC prepared during the fabrication of the solar cells. A schematic of the layer stacks in the tandem measurement setup is depicted in Fig. 5 in the appendix. The perovskite filters have the same structure and optical properties as that of the semitransparent perovskite solar cells. No additional material was used as a spacer between the top PSC filters and the bottom c-Si solar cells. Therefore, an air gap remains between the sub-cells. For the c-Si measured stand-alone or measured under the filters, a shadow mask is used with an aperture area of 72 mm^2 . The final PCE of the 4 T tandem configuration was obtained by the addition of the top PSC PCE to the bottom c-Si solar cell (under the different filters) PCE. Cross-sectional scanning electron microscopy was performed using a Zeiss Crossbeam 1540 EsB scanning electron microscope. Focused ion beam with a gallium source was used for creating a cut through the entire sample. 1-2 keV was typically used for capturing an image. The transmittance and reflectance measurements were performed using a PerkinElmer Lambda 1050 spectrophotometer. External quantum efficiency (EQE) measurements were performed using Bentham PVE300 system. A chopping frequency of

around 930 Hz with an integration of 500 ms was used to obtain the spectra. The devices were not subjected to any pre-conditioning.

3. Results and discussion

The nanostructured front electrodes are fabricated by processing self-assembled polystyrene nanopillars on a glass substrate using polymer blend lithography [43] and by the subsequent sputter deposition of the ITO electrode forming the nanostructured ITO (NS ITO). Due to the predominantly conformal growth of the ITO, corrugated ITO nanostructures are obtained (see Fig. 1(a)). Further details about the optimization of the NS ITO electrodes are described later in section 3.2. As a reference, planar ITO electrodes of the same thickness (~135 nm) are fabricated (see Fig. 6). The architecture of the PSC deposited on these electrodes consists of SnO_2 -np, $\text{Cs}_{0.1}(\text{MA}_{0.17}\text{FA}_{0.83})_{0.9}\text{Pb}(\text{I}_{0.83}\text{Br}_{0.17})_3$, spiro-MeOTAD, MoO_x , and an ITO rear electrode. More details on the fabrication sequence are given in the experimental section.

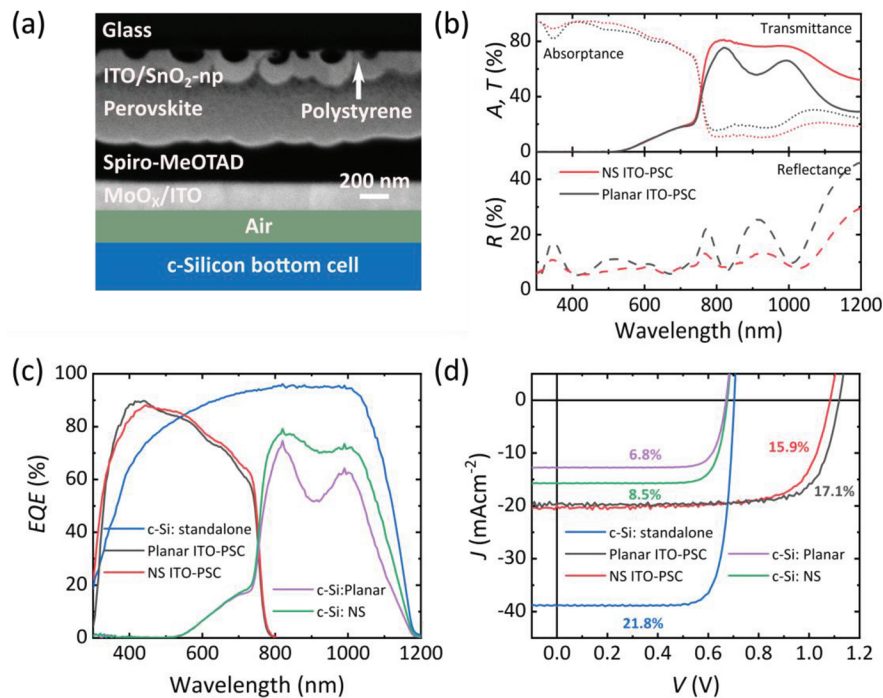


Fig. 1. (a) Cross-sectional scanning electron microscopy image of the semi-transparent perovskite solar cell fabricated on nanostructured ITO. Schematic of an air gap and a bottom c-Si solar cell is also illustrated. (b) Transmittance T , reflectance R and absorbance A for planar and nanostructured ITO based semi-transparent perovskite solar cell filters. (c) External quantum efficiency (EQE) and (d) Current density - voltage J - V characteristic of the perovskite solar cells with nanostructured ITO, perovskite solar cells with planar ITO, stand-alone c-Si solar cell, and c-Si solar cell measured below planar and nanostructured ITO perovskite solar cells.

3.1. Photovoltaic performance

The semi-transparent PSC fabricated on optimized NS ITO electrode exhibits reduced light reflection at the front interface along with improved light in-coupling within the layers (see

Fig. 1(b)). In comparison to the planar ITO reference electrode, the interferences in transmittance and in reflectance spectra are reduced, resulting in an improved optical response for the NS ITO electrode. For the top PSC, this translates into an enhanced *EQE* over a broad spectral range, from 450 nm to 780 nm (see Fig. 1(c)). The poor *EQE* response up to around 350 nm is attributed to the parasitic absorption from ITO. The additional discrepancy between the *EQE* and the absorbance in the wavelength range 650 nm – 780 nm is might be related to parasitic absorption within the layer stack. Overall, an improvement of ~2% (relative) in the J_{SC} is achieved for the PSC using the NS ITO electrode (NS ITO-PSC), leading to a PCE of 15.9% (see Fig. 1(d)) for the champion device. The statistics of 6 samples fabricated in two separate batches for two different bandgaps depicts a consistent improvement in the J_{SC} (see Fig. 7 and compare Figs. 1(c)–1(d) and Fig. 8). The small improvement in the J_{SC} for the top PSC is due to a minor reduction of the reflection losses above the bandgap of the perovskite absorber, which accounts to only 0.6 mA/cm². Even though the J_{SC} is improved, a reduction of ~40 mV in the V_{OC} is observed. Time-resolved photoluminescence measurements confirm that the lifetime of the charge carriers is reduced for the NS ITO-PSC, implying an increased non-radiative recombination (see Fig. 9) at the NS ITO/SnO₂-np or SnO₂-np/perovskite interface. Next to the V_{OC} , the FF would also be impacted by the increased non-radiative recombination. As a consequence, the PCE of the semi-transparent NS ITO-PSC is reduced compared to the planar reference PSC (planar ITO-PSC). Due to the apparent hysteresis in the *J-V* characteristics of the PSCs (see Fig. 10), the PCE of both NS ITO-PSC and planar ITO-PSC are measured under constant illumination and at constant voltage near the maximum power point to estimate the real performance of the solar cells. It is observed that the NS ITO-PSC shows stable device performance similar to the planar ITO-PSC, leading to a PCE of ~15% at the end of 5 min (see Fig. 11).

Having demonstrated stable performance in power output of the NS ITO-PSC, the prospects of mechanically-stacked 4 T perovskite/c-Si tandem solar cells are studied. Therefore, filter of semi-transparent NS ITO-PSCs and planar ITO-PSCs are stacked (without any additional material as a spacer) on top of an interdigitated back contact (IBC) c-Si solar cell (stand-alone PCE of 21.8%, schematic shown in Fig. 12) that has an optimized anti-reflection coating for the 4 T tandem configuration. In the 4 T NS ITO-PSC/c-Si tandem configuration, the c-Si bottom solar cell yields a PCE of 8.5% (c-Si: NS in Fig. 1). Compared to the planar reference, an increase in absolute PCE of 1.7% is achieved. The overall PCE of the NS ITO-PSC/c-Si tandem solar cell is 24.4% (see Table 1). The improvement in the PCE of the c-Si bottom solar cell with the NS ITO compared to the planar reference is a result of enhanced transmittance due to the reduced reflectance and absorbance of the low energy photons (see Fig. 1(b)). Thus, the *EQE* is enhanced for the entire range of wavelengths (780 nm – 1200 nm), leading to an enhancement in J_{SC} up to 2.9 mA/cm² (~23% relative) in the bottom c-Si solar cell using the NS ITO electrode. In this range, the haze in the transmission of the NS ITO electrode stands ~1% and hence, the gain is mostly achieved through better light in-coupling (see Fig. 14). The improvement in the sum of J_{SC} generated by the top and the bottom cell is relatively ~10% higher for the NS ITO-PSC/c-Si tandem solar cell compared to the planar ITO-PSC/c-Si. This exceeds the enhancement observed by Jaysankar *et al.* (3.2% relative) in 4 T perovskite/c-Si tandem modules, which incorporated an inverted pyramidal micro-texture at the air/glass interface [22]. Nevertheless, compared to the planar ITO-PSC/c-Si tandem solar cell, the PCE of the NS ITO-PSC/c-Si tandem solar cell is enhanced only by 0.5% absolute, which is due to the lower V_{OC} and the FF of the top NS ITO-PSC compared to the planar ITO-PSC as mentioned before.

It should be noted that NS ITO electrode promises to improve the J_{SC} for both the sub-cells even though the overall improvement in the PCE for the investigated devices is minor. Therefore, in order to evaluate the potential of the NS ITO electrode in terms of 4 T tandem architecture, a brief analysis is performed to estimate the PCE. This analysis considers a similar V_{OC} and FF

Table 1. Photovoltaic parameters of the perovskite solar cells with nanostructured ITO, planar ITO, stand-alone c-Si solar cell, c-Si solar cell measured below planar and nanostructured ITO perovskite solar cells and perovskite/c-Si tandem configurations.

Parameters/ Device Architecture	Planar ITO-PSC	NS ITO-PSC	c-Si: stand-alone	c-Si: Planar	c-Si: NS	4 T Planar ITO-PSC/c-Si tandem	4 T NS ITO-PSC/c-Si tandem
V_{OC} (V)	1.12	1.08	0.70	0.67	0.67	-	-
J_{SC} (mAcm ⁻²)	19.6	20.0	38.9	12.8	15.7	-	-
FF	0.78	0.73	0.80	0.80	0.80	-	-
PCE (%)	17.1	15.9	21.8	6.8	8.5	23.9	24.4
SPCE (%)	16.0	15.0	-	-	-	22.8 ^a	23.5 ^a

^aThe stabilized power conversion efficiency (SPCE) for 4 T tandem architectures is calculated from the PCE of the top semi-transparent PSC (after 5 min) and the PCE of the bottom c-Si solar cell at the maximum power point.

for the NS ITO-PSC as the planar ITO-PSC and no hysteresis. Therefore, the PCEs of the NS ITO-PSC and planar ITO-PSC are 17.4% and 17.1%, respectively. Furthermore, the influence of the bottom solar cell's *EQE* response is also studied by weighting the *EQE* of the bottom cell with the transmission of the top PSC. For this, the c-Si solar cell with a reported PCE of 26.1% is considered that has an enhanced *EQE* (compared to this work) for the entire wavelength range 300 nm – 1200 nm [44]. Table 2 summarizes the calculated J_{SC} and the potential PCE for the c-Si (this work), c-Si from Ref. [44] (labelled as Cell A), as well as a CIGS solar cell from Ref. [45] (labelled as Cell B), both in stand-alone and 4 T tandem configuration. Since, the *EQE* of the Cell A is enhanced below the bandgap of the top PSC (compare Fig. 1(c) and Fig. 13(a) solid lines) compared to the c-Si (this work), a higher J_{SC} (3.2 mA/cm²) is achieved, leading to a filtered bottom Cell A PCE of 9.5% compared to 8.5% of c-Si (this work). Therefore, with the NS ITO-PSC, the potential PCE is increased to 27.0%, 1.1% absolute higher than the potential PCE of 25.9% for c-Si (this work). In the case of planar ITO-PSC, the calculated potential PCE is only 24.9%, which is 1.2% lower compared to the stand-alone PCE of Cell A. Thus, these calculations lay down two critical requirements of the 4 T tandem architecture: (i) a bottom solar cell with enhanced *EQE* response below the bandgap of the top PSC should be considered, so as to maximize the PCE of the tandem architecture, and (ii) the transmission of the top cell must be high (which is obtained by the NS ITO electrode and not by the planar ITO electrode) so that the J_{SC} of the bottom cell is improved and the PCE of the tandem architecture is higher than the stand-alone PCE of the sub-cells. In the case of Cell B as the bottom solar cell, a slightly reduced potential PCE of 25.2% is achieved, which is due to the higher bandgap and a weaker *EQE* response of the CIGS than the c-Si (this work) for wavelengths 800 nm – 1200 nm. In summary, for all the cases, the NS ITO based devices bear the potential to surpass the stand-alone PCE of the bottom cells as well as the PCE of the planar ITO tandem architectures.

3.2. Opto-electronic properties

3.2.1. Opto-electronic properties of the optimized nanostructured ITO electrode

In this section, the properties of the optimized glass/NS ITO electrode layer are discussed to further understand the improved performance of the NS ITO-PSC/c-Si tandem solar cell. Atomic force microscopy (AFM) image of NS ITO electrode and the SEM image show that the ITO surface exhibits the nanostructures induced by the uniformly distributed PS nanopillars (see Fig. 2(a) and Fig. 15(b)). The size distribution derived from the AFM image shows that the diameter of the optimized nanostructures varies between 25 nm - 300 nm (see Fig. 2(d)) and the average inter-distance between the nanostructures is ~210 nm. The average height of these nanostructures is ~130 nm (see Fig. 16). These tall features along with the subwavelength

inter-distance between the nanostructures induces an effective gradual matching of the refractive indices ($n_{\text{Glass}} = 1.51$; $n_{\text{PS}} = 1.59$; $n_{\text{ITO}} = 1.81$ at 600 nm), which reduces the reflection losses compared to a planar and homogeneous front electrode. Moreover, in a different experiment, it is observed that the transmission of the NS ITO electrode is higher than both the planar ITO electrode and planar PS layer sandwiched between the glass and ITO (labelled as planar PS ITO in Fig. 17). Hence, the optimized NS ITO electrode exhibits significantly reduced reflection and improved transmission for a broad range of wavelengths (see Fig. 2(e)). Compared to the planar ITO electrode, the integrated transmittance weighted by the air mass 1.5 global (AM 1.5G) spectrum between 300 nm - 1200 nm is $\sim 7\%$ relative higher for the NS ITO electrode. Therefore, an improved J_{SC} ($\sim 10\%$ relative) is achieved in the tandem solar cell with this optimized NS ITO electrode. The difference in the relative improvements between the integrated transmittance of the bare NS ITO electrode and the J_{SC} of the semi-transparent NS ITO-PSC is attributed to the difference in the optical response of the thin-film layer stacks. The increased sheet resistance, R_{sh} (see Fig. 2(f)) of the optimized NS ITO electrodes (73 ohm/sq) compared to the planar ITO electrode (27 ohm/sq) can be attributed to the increased thin-film area or a possible increased number of grain boundaries reducing the mobility of charge carriers. Furthermore, cracks appear in the ITO between the nanostructures, which may also increase the sheet resistance (compare Fig. 1(a) and Fig. 6) [46]. Nevertheless, the series resistance (R_{S}) in the J - V characteristic of the PSC is only slightly affected (R_{S} of planar ITO-PSC: 70.2 Ω and NS ITO-PSC: 81.4 Ω), indicating that the decreased conductivity is not too severe. Overall, these results suggest that NS ITO electrodes are very promising optically for the application in PSCs and tandem photovoltaics.

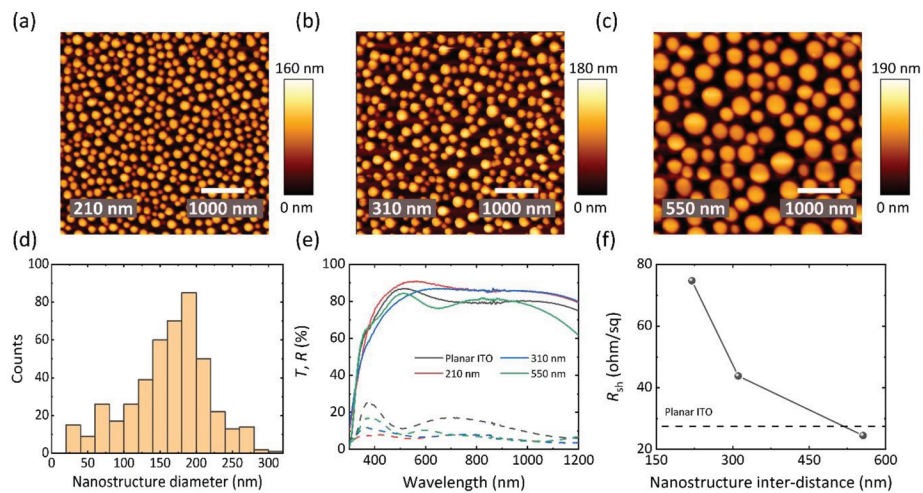


Fig. 2. Influence of the nanostructure array morphology on the opto-electrical properties of the NS ITO electrode. (a-c) Atomic force microscopy (AFM) images of the nanostructured ITO electrode for average inter-distance between the nanostructures of (a) 210 nm – optimized, (b) 310 nm and (c) 550 nm. (d) Statistical analysis of the diameter of the nanostructures in the optimized nanostructured ITO electrode derived from AFM measurement. (e) Transmittance T and reflectance R , and (f) sheet resistance (R_{sh}) of the planar ITO electrode and the NS ITO electrode for average inter-distance between the nanostructures of: 210 nm, 310 nm and 550 nm.

3.2.2. Influence of the average inter-distance between the nanostructures

The previous section presented so far illustrates the properties of the optimized NS ITO electrode and to provide a deeper insight into the key morphological parameter that influences the optical

and the electrical properties, a more systematic analysis is performed on the effect of the average inter-distance between the nanostructures. For this purpose, the average nanostructure inter-distance is varied experimentally between 210 nm and 550 nm (see Figs. 2(a)–2(c)), at the same time ensuring a similar average height of the nanostructures (110 nm - 135 nm). The various configurations of the NS ITO are obtained by altering the polymer blend mixture. Reducing the mass ratio of PS in the blend mixture leads to an increase in the average inter-distance between the nanostructures from 210 nm to 310 nm (see Figs. 2(a)–2(b)). By increasing the molecular weight of the PS, the average nanostructure inter-distance is further increased to 550 nm (see Figs. 2(b)–2(c)) [47]. It is observed that the average diameter of the nanostructures is also increased upon increasing the average nanostructure inter-distance. In terms of optical properties, a gradual increase in the reflection loss for wavelengths between 300 nm and 700 nm is observed for increased average nanostructure inter-distance (see Fig. 2(e)). Moreover, the transmission is significantly reduced. Thus, in this study, prototype NS ITO-PSCs are only fabricated for the smallest inter-distance that achieved the highest transmission. As mentioned earlier, the sheet resistance is also influenced with the addition of the nanostructures. In contrast to the optical transmission which suffers upon increased average inter-distance between the nanostructures, the sheet resistance R_{sh} on the other hand, is significantly reduced (see Fig. 2(f)). Therefore, for better conductivity, increased average inter-distance between the nanostructures is preferable. It should be noted that for small area PSCs, the increased R_{sh} notably does not affect the solar cell performance, and as a result smaller average nanostructure inter-distance would still be desired to achieve a higher transmission. However, for perovskite-based tandem mini-modules [22], where the aperture area is in the order of hundreds of mm^2 , the increased R_{sh} would substantially affect the fill-factor and hence, the device PCE. Therefore, in order to improve the electrical properties of the NS ITO electrode for perovskite-based tandem modules, further investigation is required. Possible solutions are discussed in the section 4.

3.3. Influence of incidence angle of irradiation and energy yield analysis

The key figure-of-merit for photovoltaic research is the PCE, which is determined under standard test conditions (normal incidence, temperature of 25 °C, AM 1.5G spectrum). In real world applications, solar cells experience very different irradiation conditions, given the daily and seasonal variations of the solar spectrum, weather dependent varying ratio of direct and diffuse light, and changes in the angle of incidence (AOI). In particular, nanostructured solar cells and tandem solar cell architectures are suspected to exhibit a strong angular selective response, which will impact the real world performance and the energy yield [48]. For these reasons, the influence of incidence angle on the current generation of the NS ITO-PSC/c-Si tandem architecture is investigated (see Fig. 3(a) and Table 3) [48]. The normalized J_{SC} derived from the *EQE* measurements shows that at oblique angles (AOI = 20°, 40° and 60°), the currents of the two sub-cells in the NS ITO-PSC/c-Si tandem solar cells are higher than those in the planar reference case. At AOI = 60°, the absolute gain in the J_{SC} is 3.7 mA/cm^2 . With respect to the normal incidence, this gain corresponds to an improvement in the J_{SC} by 0.4 mA/cm^2 absolute. It should also be noted that at oblique AOI, the enhancement in J_{SC} of the top PSC with NS ITO electrode is minor, but it is more pronounced in the bottom c-Si solar. At an AOI = 60°, an enhanced *EQE* and significantly reduced interference fringes are observed in the bottom c-Si solar cell filtered with the NS ITO-PSC compared to the planar ITO-PSC (see Fig. 18). These observations are in good agreement with the direct transmission of planar ITO-PSC and NS ITO-PSC carried out for a different set of samples as shown in Fig. 19. Overall, the angle dependent study implies that the NS ITO-PSC/c-Si tandem configurations enable improved current generation, both at normal and at oblique AOI. In order to quantify this improvement in terms of energy yield, an in-house simulation framework is used to determine the power output of the tandem solar cells under realistic irradiation conditions. The framework uses the irradiance based on meteorological data

for various locations in the United States of America and the external quantum efficiency data of the inspected device architecture to determine the electrical characteristics and thus, predict the energy yield. More details on the methodology can be found in Ref. [48–50]. For an optimal tilt of the solar cells, the measured optical and electrical characteristics of the NS ITO-PSC/c-Si and planar ITO-PSC/c-Si tandem configurations are calculated for different locations in various climatic zones. In order to decouple the effect of improved EQE from the overall PCE of the device and to investigate the overall potential of the NS ITO electrode on the energy yield only, the electrical properties (V_{OC} , J_{SC} and FF) of the top cells are assumed to be the same. Irrespective of the locations, the energy yield in the tandem solar cells is higher than the individual single-junction solar cells (see Fig. 3(b)). The relative enhancement in energy yield for the NS ITO-PSC/c-Si tandem solar cell is +10% than the planar ITO-PSC/c-Si. It should be noted that this enhancement surpasses the enhancement in PCE measured at standard test conditions (see Table 1), due to an excellent angular selective response of the NS ITO-PSC/c-Si as discussed earlier. More details about the hourly variation of the output power is shown in Fig. 20. The output power of the individual solar cells as well as the relative gains are depicted for a particular day (January 3rd) on an hourly basis. In comparison to the planar reference case, the two sub cells of the NS ITO-PSC/c-Si tandem solar cell generate higher output power during the entire day. The relative gain in the power output of the bottom c-Si solar cell with the NS ITO-PSC is significantly higher and over 35%, both during the sunrise and the sunset with respect to the bottom c-Si solar cell with planar ITO-PSC. This is in good agreement with the improved EQE response observed at oblique angles in the presence of nanostructures. Overall, the energy yield study reveals that NS ITO electrodes bear an exciting potential to improve the generated power output of perovskite-based tandem solar cells.

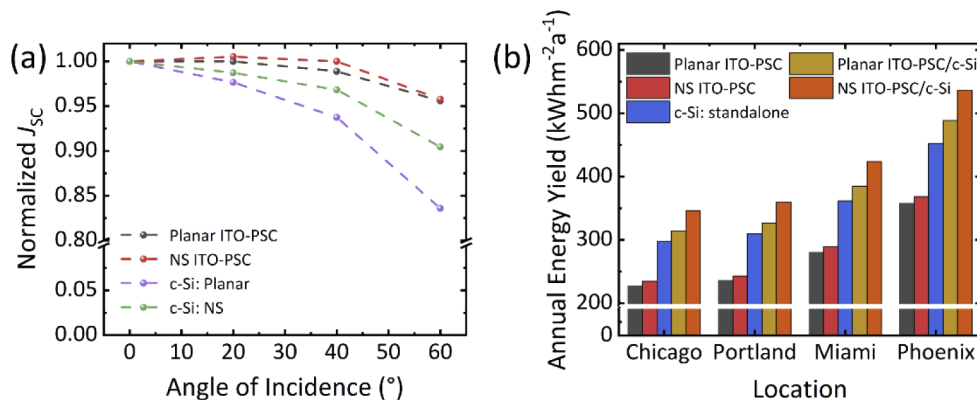


Fig. 3. (a) Normalized short-circuit current density (J_{SC}) of perovskite solar cells with nanostructured or with planar ITO, and c-Si solar cell measured below planar and nanostructured ITO perovskite solar cells for various angle of incidence. (b) Annual energy yield of the perovskite solar cells with nanostructured ITO, perovskite solar cells with planar ITO, stand-alone c-Si solar cell, and perovskite/c-Si tandem configurations for various (representative) locations in the United States of America.

4. Outlook

This work reports on NS ITO electrodes that demonstrate improved light in-coupling in prototype 4T perovskite/c-Si tandem solar cells, resulting in a moderate improvement in the J_{SC} for the top PSC and a very significant increase in J_{SC} of $\sim 23\%$ relative for the bottom c-Si solar cell. Thereby, an alternative light management concept is introduced that bears the potential to advance perovskite-based tandem photovoltaics compared to the established micron-scale light

management textures and anti-reflection coating layer. In order to exploit the full potential of NS ITO electrodes for perovskite-based tandem modules, some remaining challenges related to: (i) V_{OC} loss, (ii) upscaling, and (iii) transferring the texture to the glass substrate should be addressed. With regard to the V_{OC} loss, an alternative strategy must be explored in the fabrication of the PSCs to improve the NS ITO/ETL/perovskite interface. Thermal evaporation of the ETL can be investigated as an alternate method to deposit the ETL [51]. Next, the deposition conditions of the ITO must be optimized to avoid formation of cracks in the NS ITO electrode, which may have resulted in increased sheet resistance for smaller inter-distance between the nanostructures. Alternatively, metal grids can also be applied to reduce the sheet resistance as discussed in Ref. [9,14]. Both of this would be of high importance for the upscaling of the active area in the PSCs and deployment in real 4-terminal perovskite/c-Si tandem solar cell modules. Furthermore, different strategies should be employed to transfer the nanostructures in the glass substrate [52,53], thus circumventing the usage of PS, which limits the processing temperature of the PSC [54] and long-term stability. Moreover, optical simulations should also be employed to optimize the geometry of the nanostructures, to further minimize the losses and improve both light in-coupling and transmission of top PSCs.

5. Conclusion

In this contribution, NS ITO electrodes for perovskite/c-Si tandem solar cells are developed by sputtering ITO on self-assembled polystyrene nanopillars. NS ITO of various average nanostructure inter-distances are fabricated and optimized for reduced reflectance and increased transmittance, with a tradeoff in the increased sheet resistance. In comparison to the planar ITO electrodes, the optimized NS ITO electrodes reduce the front side reflectance and enhance the optical transmittance ($\sim 7\%$ relative) over a broad range of wavelengths (300–1200 nm). Semi-transparent PSCs fabricated on top of the NS ITO depict an increase in the J_{SC} of $\sim 2\%$ (relative), nevertheless a reduction in the V_{OC} and the FF are observed. However, improved transmission is observed for the low energy photons that leads to an additional 2.9 mA/cm^2 ($\sim 23\%$ relative) current density in the bottom c-Si solar cell, enhancing the PCE of the bottom c-Si solar cell by 1.7% absolute. Furthermore, with NS ITO as the front electrode, the perovskite/c-Si tandem solar cells are more robust towards variation in the AOI of the incident light and hence, an improved energy yield ($+10\%$ relative) is achieved. The prospective of the NS ITO is not limited to perovskite/c-Si tandem photovoltaics, but also can be implemented in other architectures such as perovskite/CIGS or perovskite/perovskite tandem solar cells, thus enabling advancement in these technologies as well.

Appendix – additional figures and tables

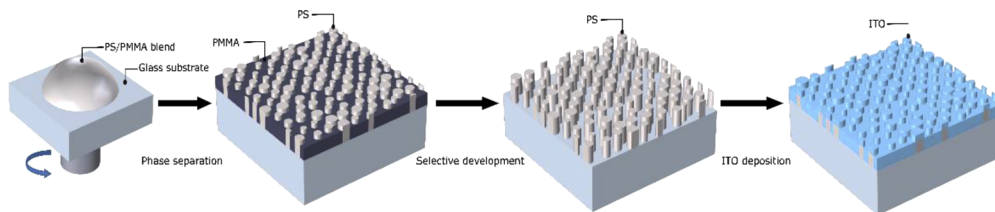


Fig. 4. Schematic of the fabrication of nanostructured ITO.

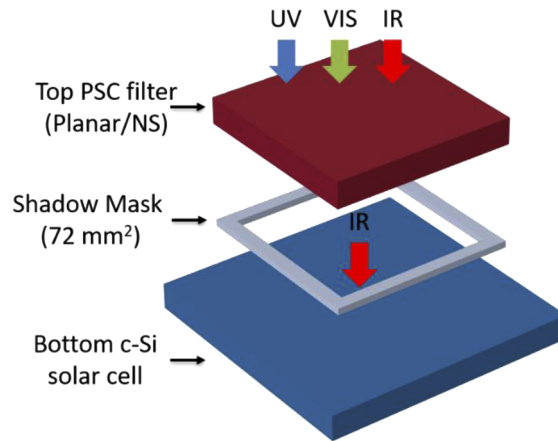


Fig. 5. Schematic illustration of the measurement of bottom c-Si solar cell using semitransparent filters of planar ITO-PSC and NS ITO-PSC for the 4 T tandem architecture.

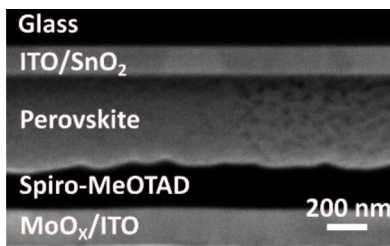


Fig. 6. Cross-sectional scanning electron microscopy (SEM) image of the perovskite solar cell: glass/planar ITO/SnO₂-np/perovskite/spiro-MeOTAD/MoO_x/ITO.

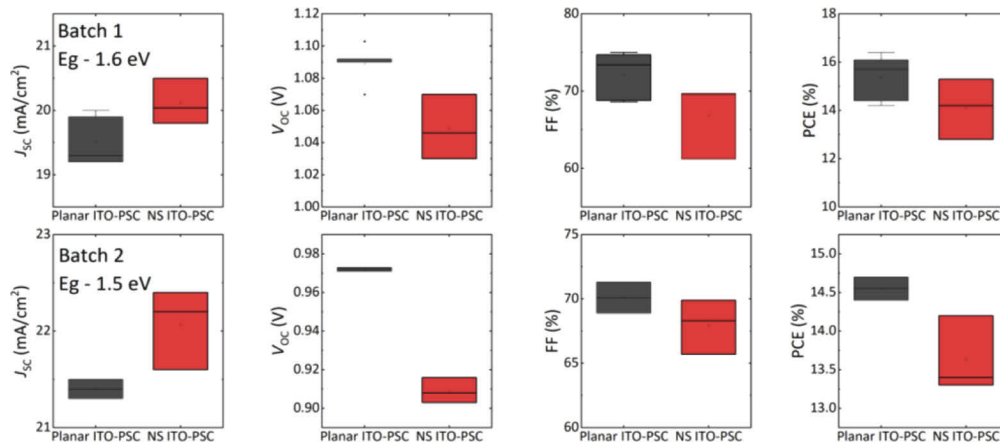


Fig. 7. Statistical distribution of short-circuit current density (J_{SC}), open-circuit voltage (V_{OC}), fill factor (FF) and the power conversion efficiency (PCE) for perovskite solar cells (PSCs) with planar and nanostructured ITO.

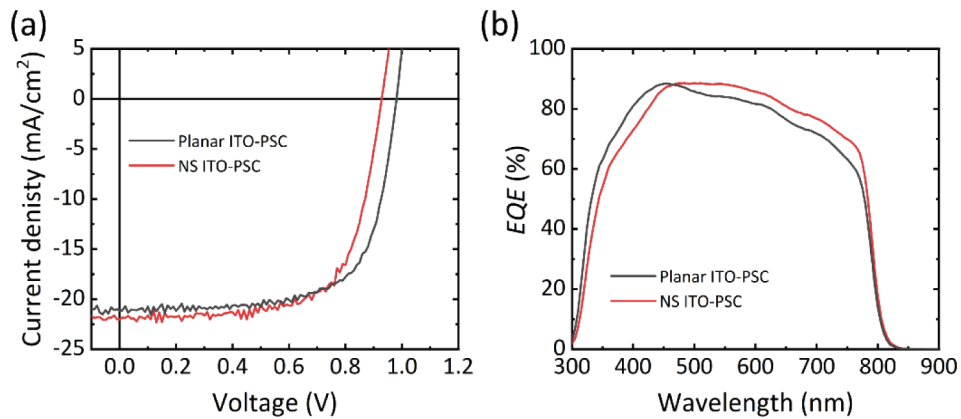


Fig. 8. (a) Current density-voltage (J - V) characteristic and (b) external quantum efficiency (EQE) of the perovskite solar cells (PSCs) with nanostructured ITO, and PSCs with planar ITO for Batch 2.

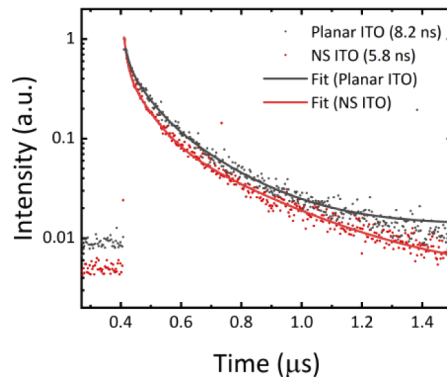


Fig. 9. Time-resolved photoluminescence spectroscopy of planar ITO and NS ITO based solar cells. During these measurements, the samples are excited with pulsed laser with an excitation wavelength of 532 nm. It is observed that the lifetime (τ) is reduced in the presence of NS ITO, which indicates higher non-radiative recombination losses in devices with NS ITO compared to the planar ITO.

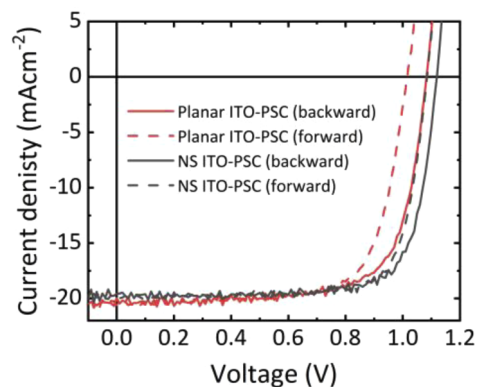


Fig. 10. Current density - voltage characteristic of the perovskite solar cells with nanostructured ITO, perovskite solar cells with planar ITO for backward and forward scan directions.

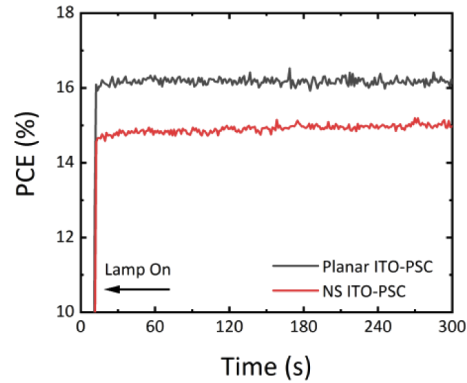


Fig. 11. Power conversion efficiency (PCE) of perovskite solar cell (PSC) with planar and nanostructured ITO measured at constant voltage near the maximum power point shows stable output power achieved by both these devices.

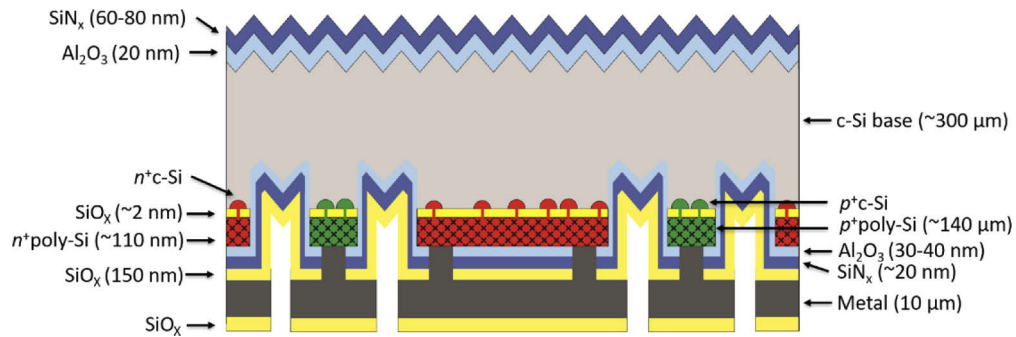


Fig. 12. Schematic of the c-Si bottom cell.

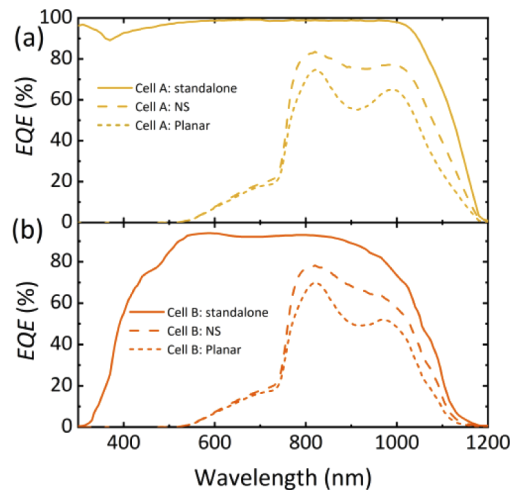


Fig. 13. External quantum efficiency (*EQE*) of stand-alone (a) c-Si solar cell (Cell A) adapted from Ref. [45] and (b) CIGS (Cell B) adapted from Ref. [46]. The *EQE* response of the same solar cells under planar ITO-PSC and NS ITO-PSC. Reproduced with permission.

Table 2. The short-circuit current density and the potential power conversion efficiency (PCE) of various bottom cells filtered with planar ITO-PSC and NS ITO-PSC.

	J_{SC} (mA/cm ²)			Potential PCE (%)				
	Stand-alone	Filtered with Planar ITO	Filtered with NS ITO	Stand-alone	Filtered with Planar ITO	Filtered with NS ITO	Planar ITO-PSC/bottom cell	NS ITO-PSC/bottom cell
Planar ITO-PSC	19.6	—	—	17.1^a	—	—	—	—
NS ITO-PSC	20.0	—	—	17.4^a	—	—	—	—
c-Si (this work)	38.9	12.8	15.7	21.8	6.8	8.5	23.9^d	25.9^e
Cell A (c-Si [45])	42.6	13.2 ^f	16.4 ^f	26.1	7.8 ^b	9.6 ^b	24.9^d	27.0^e
Cell B (CIGS [46])	35.9	11.2 ^f	13.7 ^f	21.7	6.4 ^c	7.8 ^c	23.5^d	25.2^e

^aThe PCE of the top semi-transparent Planar ITO-PSC and NS ITO-PSC is estimated considering the NS ITO-PSC has the same V_{OC} and FF as the planar ITO-PSC and no hysteresis. The following parameters are considered to calculate the PCE for:

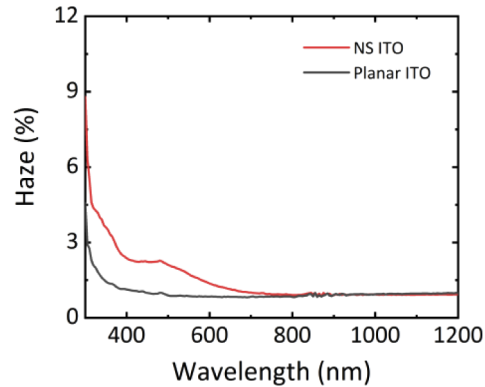
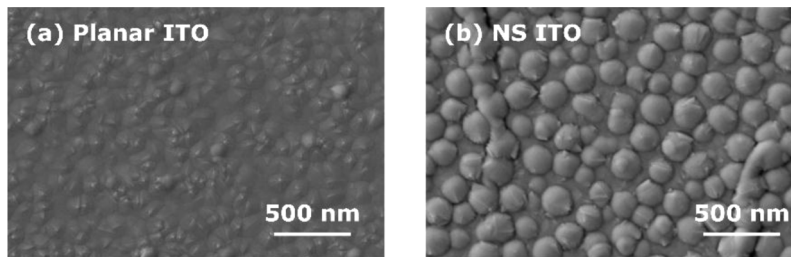
^bCell A (c-Si) [45]: FF - 0.843; V_{OC} - 0.697 V and

^cCell B (CIGS) [46]: FF - 0.793; V_{OC} - 0.716 V.

^dSum of the PCEs of Planar ITO-PSC and bottom cell.

^eSum of the PCEs of NS ITO-PSC and bottom cell.

^fThe J_{SC} is calculated by weighting the EQE of the stand-alone cells with the transmission of the respective filters.

**Fig. 14.** Haze of planar and nanostructured ITO electrodes measured on Glass/ITO substrates.**Fig. 15.** Scanning electron microscopy (SEM) image of: (a) Planar ITO electrode and (b) NS ITO electrode.

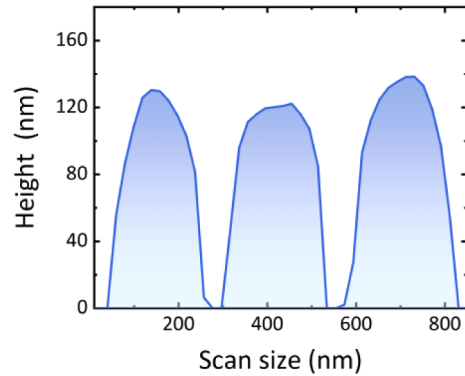


Fig. 16. The vertical profile extracted from atomic force microscopy (AFM) image of three nanostructures with representative polystyrene nanopillars coated with ITO.

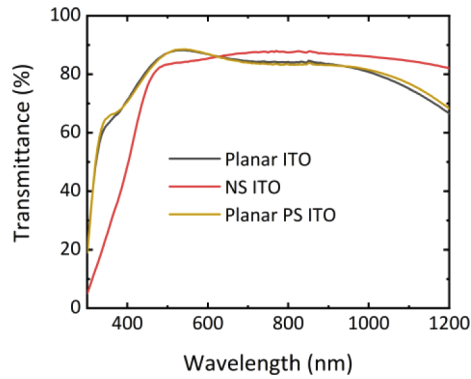


Fig. 17. Transmittance planar ITO electrode, NS ITO electrode (~300 nm inter-distance) and planar PS ITO electrode.

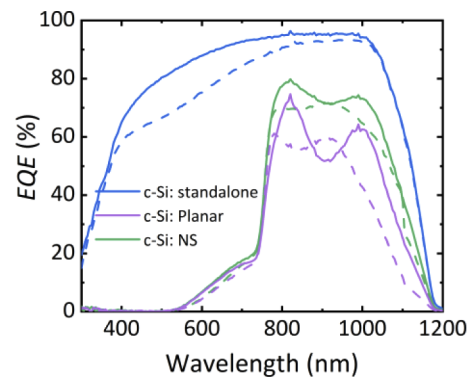


Fig. 18. External quantum efficiency (*EQE*) of stand-alone c-Si solar cell, c-Si solar cell measured under planar and nanostructured ITO perovskite solar cells for angles of incidence 0° (solid) and 60° (dashed).

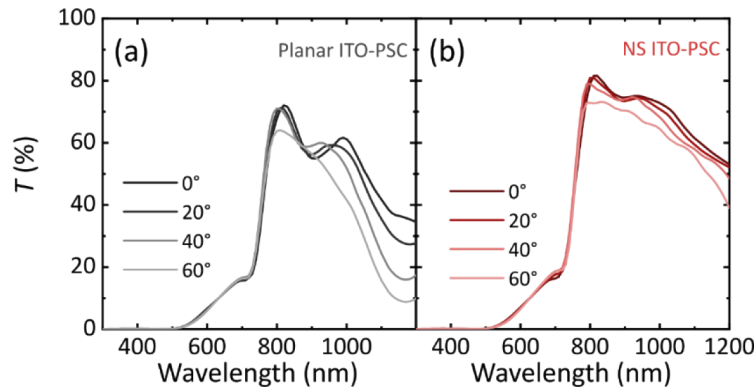


Fig. 19. Direct transmittance of (a) planar ITO-PSC and (b) NS ITO-PSC for various angles of incidence: 0°, 20°, 40° and 60°.

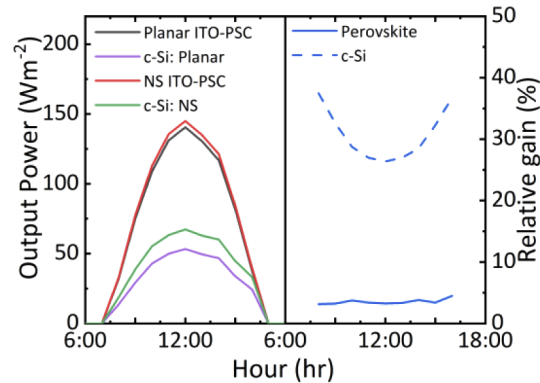


Fig. 20. Left panel: Output power estimated from energy yield for perovskite solar cell with NS ITO (NS ITO-PSC), perovskite solar cell with planar ITO (planar ITO-PSC), c-Si solar cell measured under planar ITO-PSC (c-Si: Planar) and NS ITO-PSC (c-Si: NS). Right panel: The relative gains of the sub-cells in NS ITO-PSC/c-Si tandem solar cell compared to planar ITO-PSC/c-Si tandem solar cell.

Table 3. The absolute short-circuit current density for various device architectures measured for angles of incidence (AOI) 0° and at 60°.

Device Architecture	Short-circuit current density, J_{SC} (mAcm^{-2})	
	AOI = 0°	AOI = 60°
c-Si: stand-alone	38.4	35.2
Planar ITO-PSC	18.4	17.8
NS ITO-PSC	18.9	17.9
c-Si: Planar	12.8	10.7
c-Si: NS	15.6	14.3
Total current of planar ITO-PSC/c-Si tandem solar cell	31.2	28.5
Total current of NS ITO-PSC/c-Si tandem solar cell	34.5	32.2

Funding

Helmholtz Association (HYIG of Dr. U.W. Paetzold [VH-NG-1148]; Recruitment Initiative of Prof. B.S. Richards; HEMF, PEROSEED [ZT-0024] Innovationpool, Science and Technology of Nanosystems); KIT Young Investigator Network; Bundesministerium für Bildung und Forschung (PRINTPERO [03SF0557A]); Deutsche Forschungsgemeinschaft (LAMBDA); Bundesministerium für Wirtschaft und Technologie (“EASi” (FKZ0324040)); German State of Lower Saxony.

Acknowledgments

The authors express their gratitude towards the great spirit of the “KIT perovskite PV taskforce”, especially Isabel Allegro, Diana Rueda-Delgado, Adrian Mertens, Tobias Abzieher, Bahram Abdollahi Nejang and Saba Gharibzadeh. We also acknowledge Patrice Brenner for the focused ion beam cut of the perovskite solar cells. The authors wish to thank H. Kohlenberg and the team from ISFH and from Institute of Electronic Materials and Devices (MBE) at Leibniz Universität Hannover for the Si bottom cell fabrication. The authors gratefully acknowledge the help and support of the Karlsruhe School of Optics & Photonics (KSOP) and Max Planck School of Photonics (MPSP), respectively.

Disclosures

The authors declare no conflicts of interest.

References

1. NREL, “NREL Efficiency Chart,” <https://www.nrel.gov/pv/cell-efficiency.html>.
2. S. De Wolf, J. Holovsky, S. J. Moon, P. Löper, B. Niesen, M. Ledinsky, F. J. Haug, J. H. Yum, and C. Ballif, “Organometallic halide perovskites: Sharp optical absorption edge and its relation to photovoltaic performance,” *J. Phys. Chem. Lett.* **5**(6), 1035–1039 (2014).
3. S. D. Stranks, G. E. Eperon, G. Grancini, C. Menelaou, M. J. P. Alcocer, T. Leijtens, L. M. Herz, A. Petrozza, and H. J. Snaith, “Electron-hole diffusion lengths exceeding 1 micrometer in an organometal trihalide perovskite absorber,” *Science* **342**(6156), 341–344 (2013).
4. P. Brenner, T. Glöckler, D. Rueda-Delgado, T. Abzieher, M. Jakoby, B. S. Richards, U. W. Paetzold, I. A. Howard, and U. Lemmer, “Triple cation mixed-halide perovskites for tunable lasers,” *Opt. Mater. Express* **7**(11), 4082 (2017).
5. S. Rühle, “The detailed balance limit of perovskite/silicon and perovskite/CdTe tandem solar cells,” *Phys. Status Solidi A* **214**(5), 1600955 (2017).
6. A. De Vos, “Detailed balance limit of the efficiency of tandem solar cells,” *J. Phys. D: Appl. Phys.* **13**(5), 839–846 (1980).
7. A. S. Brown and M. A. Green, “Detailed balance limit for the series constrained two terminal tandem solar cell,” *Phys. E* **14**(1-2), 96–100 (2002).
8. T. Duong, Y. Wu, H. Shen, J. Peng, X. Fu, D. Jacobs, E.-C. Wang, T. C. Kho, K. C. Fong, M. Stocks, E. Franklin, A. Blakers, N. Zin, K. McIntosh, W. Li, Y.-B. Cheng, T. P. White, K. Weber, and K. Catchpole, “Rubidium Multication Perovskite with Optimized Bandgap for Perovskite-Silicon Tandem with over 26% Efficiency,” *Adv. Energy Mater.* **7**(14), 1700228 (2017).
9. H. Shen, T. Duong, J. Peng, D. Jacobs, N. Wu, J. Gong, Y. Wu, S. K. Karuturi, X. Fu, K. Weber, X. Xiao, T. P. White, and K. Catchpole, “Mechanically-stacked perovskite/CIGS tandem solar cells with efficiency of 23.9% and reduced oxygen sensitivity,” *Energy Environ. Sci.* **11**(2), 394–406 (2018).
10. D. Zhang, M. Najafi, V. Zardetto, M. Dörenkämper, X. Zhou, S. Veenstra, L. J. Geerligs, T. Aernouts, and R. Andriessen, “High efficiency 4-terminal perovskite/c-Si tandem cells,” *Sol. Energy Mater. Sol. Cells* **188**(July), 1–5 (2018).
11. E. Aydin, M. De Bastiani, X. Yang, M. Sajjad, F. Aljamaan, Y. Smirnov, M. N. Hedhili, W. Liu, T. G. Allen, L. Xu, E. Van Kerschaver, M. Morales-Masis, U. Schwingenschlögl, and S. De Wolf, “Zr-Doped Indium Oxide (IZRO) Transparent Electrodes for Perovskite-Based Tandem Solar Cells,” *Adv. Funct. Mater.* **29**(25), 1901741–10 (2019).
12. N. N. Lal, Y. Dkhissi, W. Li, Q. Hou, Y. B. Cheng, and U. Bach, “Perovskite Tandem Solar Cells,” *Adv. Energy Mater.* **7**(18), 1–18 (2017).
13. J. Werner, B. Niesen, and C. Ballif, “Perovskite/Silicon Tandem Solar Cells: Marriage of Convenience or True Love Story? - An Overview,” *Adv. Mater. Interfaces* **5**(1), 1700731 (2018).

14. D. A. Jacobs, M. Langenhorst, F. Sahli, B. S. Richards, T. P. White, C. Ballif, K. R. Catchpole, and U. W. Paetzold, "Light Management: A Key Concept in High-Efficiency Perovskite/Silicon Tandem Photovoltaics," *J. Phys. Chem. Lett.* **10**(11), 3159–3170 (2019).
15. T. Duong, N. Lal, D. Grant, D. Jacobs, P. Zheng, S. Rahman, H. Shen, M. Stocks, A. Blakers, K. Weber, T. P. White, and K. R. Catchpole, "Semitransparent Perovskite Solar Cell With Sputtered Front and Rear Electrodes for a Four-Terminal Tandem," *IEEE J. Photovoltaics* **6**(3), 679–687 (2016).
16. C. D. Bailie, M. G. Christoforo, J. P. Mailoa, A. R. Bowering, E. L. Unger, W. H. Nguyen, J. Burschka, N. Pellet, R. Nou, T. Buonassisi, A. Salleo, J. Z. Lee, M. Grätzel, R. Noufi, T. Buonassisi, A. Salleo, and M. D. McGehee, "Semi-transparent perovskite solar cells for tandems with silicon and CIGS," *Energy Environ. Sci.* **8**(3), 956–963 (2015).
17. C. Wehrenfennig, G. E. Eperon, M. B. Johnston, H. J. Snaith, and L. M. Herz, "High charge carrier mobilities and lifetimes in organolead trihalide perovskites," *Adv. Mater.* **26**(10), 1584–1589 (2014).
18. J. P. C. Baena, L. Steier, W. Tress, M. Saliba, S. Neutzner, T. Matsui, F. Giordano, T. J. Jacobsson, A. R. S. Kandada, S. M. Zakeeruddin, A. Petrozza, A. Abate, M. K. Nazeeruddin, M. Grätzel, and A. Hagfeldt, "Highly efficient planar perovskite solar cells through band alignment engineering," *Energy Environ. Sci.* **8**(10), 2928–2934 (2015).
19. F. Sahli, J. Werner, B. A. Kamino, M. Bräuninger, R. Monnard, B. Paviet-Salomon, L. Barraud, L. Ding, J. J. Diaz Leon, D. Sacchetto, G. Cattaneo, M. Despeisse, M. Boccard, S. Nicolay, Q. Jeangros, B. Niesen, and C. Ballif, "Fully textured monolithic perovskite/silicon tandem solar cells with 25.2% power conversion efficiency," *Nat. Mater.* **17**(9), 820–826 (2018).
20. J. Werner, L. Barraud, A. Walter, M. Bräuninger, F. Sahli, D. Sacchetto, N. Tétreault, B. Paviet-Salomon, S. J. Moon, C. Allebé, M. Despeisse, S. Nicolay, S. De Wolf, B. Niesen, and C. Ballif, "Efficient Near-Infrared-Transparent Perovskite Solar Cells Enabling Direct Comparison of 4-Terminal and Monolithic Perovskite/Silicon Tandem Cells," *ACS Energy Lett.* **1**(2), 474–480 (2016).
21. M. Jošt, E. Köhnen, A. B. Morales-Vilches, B. Lipovšek, K. Jäger, B. Macco, A. Al-Ashouri, J. Krč, L. Korte, B. Rech, R. Schlattmann, M. Topič, B. Stannowski, and S. Albrecht, "Textured interfaces in monolithic perovskite/silicon tandem solar cells: Advanced light management for improved efficiency and energy yield," *Energy Environ. Sci.* **11**(12), 3511–3523 (2018).
22. M. Jaysankar, M. Filipič, B. Zielinski, R. Schmager, W. Song, W. Qiu, U. W. Paetzold, T. Aernouts, M. Debucquoy, R. Gehlhaar, and J. Poortmans, "Perovskite-silicon tandem solar modules with optimised light harvesting," *Energy Environ. Sci.* **11**(6), 1489–1498 (2018).
23. A. Deinega, I. Valuev, B. Potapkin, and Y. Lozovik, "Minimizing light reflection from dielectric textured surfaces," *J. Opt. Soc. Am. A* **28**(5), 770 (2011).
24. B. W. Schneider, N. N. Lal, S. Baker-Finch, and T. P. White, "Pyramidal surface textures for light trapping and antireflection in perovskite-on-silicon tandem solar cells," *Opt. Express* **22**(S6), A1422 (2014).
25. R. Schmager, B. Fritz, R. Hünig, K. Ding, U. Lemmer, B. S. Richards, G. Gomard, and U. W. Paetzold, "Texture of the Viola Flower for Light Harvesting in Photovoltaics," *ACS Photonics* **4**(11), 2687–2692 (2017).
26. R. Schmager, G. Gomard, B. S. Richards, and U. W. Paetzold, "Nanophotonic perovskite layers for enhanced current generation and mitigation of lead in perovskite solar cells," *Sol. Energy Mater. Sol. Cells* **192**(2019), 65–71 (2019).
27. D. Chen, P. Manley, P. Tockhorn, D. Eisenhauer, G. Köppel, M. Hammerschmidt, S. Burger, S. Albrecht, C. Becker, and K. Jäger, "Nanophotonic Light Management for Perovskite-Silicon Tandem Solar Cells," *J. Photonics Energy* **8**(2), 1–14 (2018).
28. M. M. Tavakoli, Q. Lin, S.-F. F. Leung, G. C. Lui, H. Lu, L. Li, B. Xiang, and Z. Fan, "Efficient, flexible and mechanically robust perovskite solar cells on inverted nanocone plastic substrates," *Nanoscale* **8**(7), 4276–4283 (2016).
29. S. Liu, L. Wang, Y. Luo, F. So, and N. Barange, "Perovskite Solar Cells on Corrugated Substrates with Enhanced Efficiency," *Small* **12**(46), 6346–6352 (2016).
30. U. W. Paetzold, W. Qiu, F. Finger, J. Poortmans, and D. Cheyons, "Nanophotonic front electrodes for perovskite solar cells," *Appl. Phys. Lett.* **106**(17), 173101 (2015).
31. J. Wei, R. P. Xu, Y. Q. Li, C. Li, J. De Chen, X. D. Zhao, Z. Z. Xie, C. S. Lee, W. J. Zhang, and J. X. Tang, "Enhanced Light Harvesting in Perovskite Solar Cells by a Bioinspired Nanostructured Back Electrode," *Adv. Energy Mater.* **7**(20), 1–7 (2017).
32. H. Zhang, M. Kramarenko, J. Osmond, J. Toudert, and J. Martorell, "Natural Random Nanotexturing of the Au Interface for Light Backscattering Enhanced Performance in Perovskite Solar Cells," *ACS Photonics* **5**(6), 2243–2250 (2018).
33. S. Jang, J. Yoon, K. Ha, M. cheol Kim, D. H. Kim, S. M. Kim, S. M. Kang, S. J. Park, H. S. Jung, and M. Choi, "Facile fabrication of three-dimensional TiO₂ structures for highly efficient perovskite solar cells," *Nano Energy* **22**, 499–506 (2016).
34. X. Zheng, Z. Wei, H. Chen, Q. Zhang, H. He, S. Xiao, Z. Fan, K. S. Wong, and S. Yang, "Designing nanobowl arrays of mesoporous TiO₂ as an alternative electron transporting layer for carbon cathode-based perovskite solar cells," *Nanoscale* **8**(12), 6393–6402 (2016).
35. Y. Cheng, C. Chen, X. Chen, J. Jin, H. Li, H. Song, and Q. Dai, "Considerably enhanced perovskite solar cells via the introduction of metallic nanostructures," *J. Mater. Chem. A* **5**(14), 6515–6521 (2017).

36. K. Meng, S. Gao, L. Wu, G. Wang, X. Liu, Z. Liu, and G. Chen, "Two-Dimensional Organic-Inorganic Hybrid Perovskite Photonic Films," *Nano Lett.* **16**(7), 4166–4173 (2016).
37. Y. Wang, P. Wang, X. Zhou, C. Li, H. Li, X. Hu, F. Li, X. Liu, M. Li, and Y. Song, "Diffraction-Grated Perovskite Induced Highly Efficient Solar Cells through Nanophotonic Light Trapping," *Adv. Energy Mater.* **8**(12), 1–8 (2018).
38. I. Khan, M. Bauch, T. Dimopoulos, and J. Dostalek, "Nanostructured as-deposited indium tin oxide thin films for broadband antireflection and light trapping," *Nanotechnology* **28**(32), 325201 (2017).
39. M. Rienäcker, A. Merkle, U. Römer, H. Kohlenberg, J. Krügener, R. Brendel, and R. Peibst, "Recombination Behavior of Photolithography-free Back Junction Back Contact Solar Cells with Carrier-selective Polysilicon on Oxide Junctions for Both Polarities," *Energy Procedia* **92**, 412–418 (2016).
40. M. Rienacker, M. Bossmeyer, A. Merkle, U. Romer, F. Haase, J. Krugener, R. Brendel, and R. Peibst, "Junction resistivity of carrier selective polysilicon on oxide junctions and its impact on the solar cell performance," *2017 IEEE 44th Photovolt. Spec. Conf. PVSC 2017* **7**(1), 1–7 (2017).
41. S. Essig, C. Allebé, T. Remo, J. F. Geisz, M. A. Steiner, K. Horowitz, L. Barraud, J. S. Ward, M. Schnabel, A. Descocedres, D. L. Young, M. Woodhouse, M. Despeisse, C. Ballif, and A. Tamboli, "Raising the one-sun conversion efficiency of III-V/Si solar cells to 32.8% for two junctions and 35.9% for three junctions," *Nat. Energy* **2**(9), 17144 (2017).
42. M. Schnabel, N. Renewable, E. L. Warren, N. Renewable, and A. Merkle, "Mechanically Stacked Dual-Junction and Triple-Junction III-V/Si-IBC Cells with Efficiencies of 31.5% and 35.4%," (November), (2017).
43. Y. J. Donie, M. Smeets, K. Bittkau, A. Mertens, J. B. Preinfalk, V. Smirnov, U. Lemmer, A. Egel, F. Lentz, G. Gomard, J. B. Preinfalk, A. Mertens, V. Smirnov, U. Lemmer, K. Bittkau, and G. Gomard, "Light trapping in thin film silicon solar cells: Via phase separated disordered nanopillars," *Nanoscale* **10**(14), 6651–6659 (2018).
44. F. Haase, C. Hollemann, S. Schäfer, A. Merkle, M. Rienäcker, J. Krügener, R. Brendel, and R. Peibst, "Laser contact openings for local poly-Si-metal contacts enabling 26.1%-efficient POLO-IBC solar cells," *Sol. Energy Mater. Sol. Cells* **186**(June), 184–193 (2018).
45. P. Jackson, D. Hariskos, R. Wuerz, O. Kiowski, A. Bauer, T. M. Friedlmeier, and M. Powalla, "Properties of Cu(In,Ga)Se₂ solar cells with new record efficiencies up to 21.7%," *Phys. Status Solidi RRL* **9**(1), 28–31 (2015).
46. M. Python, O. Madani, D. Dominé, F. Meillaud, E. Vallat-Sauvain, and C. Ballif, "Influence of the substrate geometrical parameters on microcrystalline silicon growth for thin-film solar cells," *Sol. Energy Mater. Sol. Cells* **93**(10), 1714–1720 (2009).
47. C. Huang, M. Moosmann, J. Jin, T. Heiler, S. Walheim, and T. Schimme, "Polymer blend lithography: A versatile method to fabricate nanopatterned self-assembled monolayers," *Beilstein J. Nanotechnol.* **3**(1), 620–628 (2012).
48. J. Lehr, M. Langenhorst, R. Schmager, S. Kirner, U. Lemmer, B. S. Richards, C. Case, and U. W. Paetzold, "Energy yield modelling of perovskite/silicon two-terminal tandem PV modules with flat and textured interfaces," *Sustainable Energy Fuels* **2**(12), 2754–2761 (2018).
49. M. Langenhorst, B. Sautter, R. Schmager, J. Lehr, E. Ahlswede, M. Powalla, U. Lemmer, B. S. Richards, and U. W. Paetzold, "Energy yield of all thin-film perovskite/CIGS tandem solar modules," *Prog. Photovoltaics* **27**(4), 290–298 (2019).
50. R. Schmager, M. Langenhorst, J. Lehr, U. Lemmer, B. S. Richards, and U. W. Paetzold, "Methodology of energy yield modelling of perovskite-based multi-junction photovoltaics," *Opt. Express* **27**(8), A507 (2019).
51. E. Köhnen, M. Jošt, A. B. Morales-Vilches, P. Tockhorn, A. Al-Ashouri, B. Macco, L. Kegelmann, L. Korte, B. Rech, R. Schlatmann, B. Stannowski, and S. Albrecht, "Highly efficient monolithic perovskite silicon tandem solar cells: Analyzing the influence of current mismatch on device performance," *Sustainable Energy Fuels* **3**(8), 1995–2005 (2019).
52. S. Ji, K. Song, T. B. Nguyen, N. Kim, and H. Lim, "Optimal moth eye nanostructure array on transparent glass towards broadband antireflection," *ACS Appl. Mater. Interfaces* **5**(21), 10731–10737 (2013).
53. M. Langenhorst, D. Ritzer, F. Kotz, P. Risch, S. Dottermusch, A. Roslizar, R. Schmager, B. S. Richards, B. E. Rapp, and U. W. Paetzold, "Liquid Glass for Photovoltaics: Multifunctional Front Cover Glass for Solar Modules," *ACS Appl. Mater. Interfaces* **11**(38), 35015–35022 (2019).
54. J. Rieger, "The glass transition temperature of polystyrene," *J. Therm. Anal.* **46**(3-4), 965–972 (1996).